A 0.31-THz Orbital-Angular-Momentum (OAM) Wave Transceiver in CMOS With Bits-to-OAM Mode Mapping

Muhammad Ibrahim Wasiq Khan, *Graduate Student Member, IEEE*,
Jongchan Woo, *Graduate Student Member, IEEE*, Xiang Yi, *Senior Member, IEEE*,
Mohamed I. Ibrahim, *Member, IEEE*, Rabia Tugce Yazicigil, *Member, IEEE*,
Anantha P. Chandrakasan, *Fellow, IEEE*, and Ruonan Han, *Senior Member, IEEE*

Abstract— **This article reports the first chip-based demonstration (at any frequency) of a transceiver front end that transmits and receives electromagnetic waves with a helical distribution of wavefront phase [namely, orbital angular momentum (OAM)]. The CMOS chip consists of eight 0.31-THz modulator/detector units, with an integrated patch antenna, which are placed in a uniform circular pattern with a diameter of one free-space wavelength. The chip transmits OAM modes that are digitally switched among the $m = 0$ (plane wave), $+1$ (left-handed), -1 (right-handed), and $(+1) + (-1)$ (superposition) states. The chip is also reconfigurable into a receiver mode that identifies different OAM modes with >10-dB rejection of mismatched modes. The array, driven by only one 310-GHz signal generation path, has a measured EIRP of −4.8 dBm and consumes 154 mW of dc power in the OAM source mode. In the receiver mode, it has a measured conversion loss of ∼30 dB and consumes 166 mW of dc power. Using a low-cost 65-nm bulk CMOS technology, the terahertz (THz)-OAM chip has an area of only 2.1 × 2.6 mm^2, which is the smallest among all prior OAM prototypes. The output OAM beam profiles and modes' orthogonality are experimentally verified. The dynamic mode switching capability of the chip is also verified in the time domain across 1-m distance, and a full-silicon OAM link is demonstrated.**

Index Terms—**Amplifier-multiplier chain, CMOS, far-field, OAM modes, orbital angular momentum (OAM), orthogonal, security, terahertz (THz), uniform circular antenna array.**

Manuscript received September 9, 2021; revised November 23, 2021 and December 30, 2021; accepted January 3, 2022. Date of publication January 25, 2022; date of current version April 25, 2022. This article was approved by Associate Editor Domine Leenaerts. This work was supported by the National Science Foundation under Grant EAGER SARE ECCS-2028824. An earlier version of this article was presented at the IEEE Radio Frequency Integrated Circuits (RFIC) Symposium, Atlanta, GA, USA, June 2021 [DOI: https://doi.org/10.1109/JSSC.2022.3141366]. *(Corresponding author: Muhammad Ibrahim Wasiq Khan.)*

Muhammad Ibrahim Wasiq Khan, Jongchan Woo, Anantha P. Chandrakasan, and Ruonan Han are with the Department of Electrical Engineering and Computer Science, Massachusetts Institute of Technology (MIT), Cambridge, MA 02139 USA (e-mail: ibrahimw@mit.edu).

Xiang Yi was with the Massachusetts Institute of Technology (MIT), Cambridge, MA 02139 USA. He is now with the School of Microelectronics, South China University of Technology, Guangzhou, China.

Mohamed I. Ibrahim was with the Massachusetts Institute of Technology (MIT), Cambridge, MA 02139 USA. He is now with MediaTek USA, Irvine, CA 92618 USA.

Rabia Tugce Yazicigil was with the Massachusetts Institute of Technology (MIT), Cambridge, MA 02139 USA. She is now with the Department of Electrical and Computer Engineering, Boston University, Boston, MA 02215 USA.

Color versions of one or more figures in this article are available at https://doi.org/10.1109/JSSC.2022.3141366.

Digital Object Identifier 10.1109/JSSC.2022.3141366

I. INTRODUCTION

MULTIPLEXING of electromagnetic (EM) waves with different frequencies, polarizations, and coding has been extensively exploited in wireless systems. Recently, another dimension of EM wave, the orbital angular momentum (OAM), is attracting increasing attention. In 1909, the idea that EM waves carry angular momentum was discussed in a work of Poynting [1], who anticipated that circularly polarized light should have angular momentum. In 1935, it was, for the first time, experimentally verified by Beth [2], [3], who demonstrated the transfer of angular momentum between polarized light and the rotational motion of a birefringent wave plate. Within the frame of paraxial approximations, this angular momentum is divided into spin-angular momentum (SAM) that is linked to circular polarization of the EM wave and OAM that characterize the rotation of the Poynting vector along the direction of propagation. The optical OAM regime gained a great renew of interest in the 1990s when the quantum characteristics of OAM states were discovered [4], [5]. However, OAM in the radio frequency band was first simulated in 2007 [6] and experimentally verified in 2011 [7].

An OAM-based wave possesses a wavefront with a helical phase distribution around the central axis of the beam with a phase singularity running along the axis. There are two classes of Gaussian beams that are known to carry OAM modes: Bessel–Gaussian (BG) beams and Laguerre–Gaussian (LG) beams. Both are solutions of the Helmholtz equation solved in cylindrical coordinates under paraxial approximation. Mathematically, LG$_{\text{pm}}$ modes are given by [8]

$$\text{LG}_{\text{pm}} = \frac{C}{\sqrt{\left(1 + z^2/z_R^2\right)}} \cdot \left[\frac{r\sqrt{2}}{w(z)}\right]^{|m|} \cdot L_p^{|m|}\left(\frac{2r^2}{w^2(z)}\right) \cdot e^{\frac{-r^2}{w^2(z)}} \cdot e^{jm\phi} \quad (1)$$

where r, ϕ, and z are coordinate variables for cylindrical coordinate system, C is a constant, $w(z) = w(0)((z^2 + z_R^2)/z_R^2)^{1/2}$ is the $1/e$ radius of the Gaussian term with $w(0)$ being the beam waist at $z = 0$, z_R is the Rayleigh range, $L_p^{|m|}(x)$ is an associated Laguerre polynomial, and p is the number of radial modes in the intensity distribution. The term $e^{jm\phi}$ represents

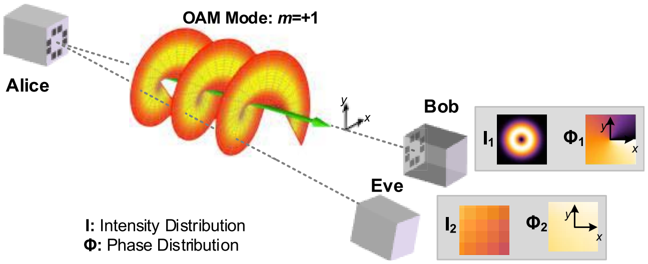

Fig. 1. Potential application of THz-OAM transceiver in physically secure wireless link against off-beam-axis eavesdropping.

the azimuthal variation of phase with m representing its index, i.e., the OAM mode. Note that the z-variation, i.e., variation in the direction of propagation, is omitted for the sake of simplicity.

Different OAM modes, determined by the handedness and the total phase change ($\phi = 2m\pi$ and $m = 0, \pm 1, \pm 2, \ldots$) of the wavefront twist, are orthogonal. Previously, multi-OAM-mode transmission has been studied for the enhancement of spectral efficiency [9]–[12]. In [9], four independent OAM beams on each of two orthogonal polarizations, modulated with 16-QAM 28-GHz signal, were multiplexed to achieve a data rate of 32 Gb/s. At 40 GHz, the work in [11] has demonstrated over 100 Gb/s using mode division multiplexing with seven OAM modes ($m = 0, \pm 1, \pm 2, \pm 3$) and dual-linear polarizations. However, it should be noted that spatial-multiplexing of OAM modes does not increase the channel capacity beyond what is achievable in multiple-input–multiple-output (MIMO) communication systems [13].

The terahertz (THz) band is enabling beyond-5G communications [14]–[18]. Large antenna arrays will be the basic building blocks for such networks similar to 5G MIMO systems. An emerging challenge is the security of these wireless links, which are susceptible to eavesdropping at unintended positions, due to beam divergence and antenna sidelobes. Traditionally, wireless communication is secured at network and application layers using digital encryption techniques that rely on the trustworthy secret key distribution. Such security architectures are becoming computationally intensive and are not scalable with ubiquitous THz-links operating at multi-Gb/s with strict energy constraints and latency requirements [19]. Physical layer security (PLS) significantly relaxes the requirements for security at other layers [20]. OAM is a potential candidate that can physically secure the one-way transmission of secret keys in such networks and is easily generated from planar antenna arrays. The instantaneous mode of an OAM beam, when driven by the bits of the secret key, encodes the information within the phase twist around the beam axis (see Fig. 1). It can only be effectively detected by a receiver with multiple phase-comparing antennas located around that axis. Such positioning requirement boosts the robustness against eavesdropping at off-axis locations [21], [22], where the SNR of the inter-antenna phase gradient rapidly drops below the detectable threshold. This makes OAM-based security unique compared to the other PLS techniques that rely on the distortion of the signal constellation at unintended directions using directional or space–time modulation [23]–[26].

Conventional OAM generation approaches involve dielectric spiral-phase plate (SPP) at optical [27] and millimeter-wave [9] frequencies, planar SPP [28], flat plate with holes [29], passive uniform circular antenna array [10], [11], [30], or metasurface in conjunction with separate signal drivers [31]. These discrete solutions, however, lead to very bulky, expensive, and power-hungry systems. Most of these systems also cannot dynamically switch between OAM modes. Up until now, no chip-based OAM component at any frequency is reported. In this article, we, for the first time, present a CMOS active antenna array that not only can generate and receive OAM waves at 310 GHz but also perform electrical OAM mode switching among the $m = +1$ (left-handed), -1 (right-handed), $(+1) + (-1)$ (superposition), and 0 (plane wave) states [32]. The above multiplexing and security applications are, therefore, made possible at the chip scale. This article is organized as follows. In Section II, the overall architecture of the chip is described. Details of the 310-GHz pixel circuits are given in Section III. Then, Section IV presents the design of the 310-GHz signal generator. The control algorithm for OAM mode mapping is discussed in Section V. After showing the experiments and demonstrations in Section VI, we conclude this article in Section VII with comparisons with the prior state of the arts.

II. THz-OAM TRANSCEIVER ARCHITECTURE

The chip architecture is shown in Fig. 2. It consists of eight THz modulator/detector units (referred to as *pixel* henceforth) driven by a 310-GHz signal generator through a power divider. The pixels, with their integrated patch antenna, are placed in a uniform circular pattern. Each pixel generates radiation with a phase difference of $\Delta\phi$ with respect to its neighboring pixels. $\Delta\phi$ is adjusted by the LO signals from the controller, and its values of 0°, +45°, and −45° correspond to the OAM modes of $m = 0$, $+1$ and -1, respectively. An on-chip controller configures the chip in either transmission or reception mode. In the transmission mode, a Keccak block generates data of a random key, which can be mapped to the instantaneous OAM modes. In the reception mode, each pixel mixes its received wave with the local 310-GHz signal and generates an IF output. Analog phase comparison of these IF signals enables the determination of the incident OAM mode.

A. Circular Antenna Array

The array factor for circular antenna array is given as

$$\mathrm{AF} = \sum_{n=0}^{N-1} I_n e^{jn\phi_n} e^{jkr_n[\cos\alpha_n \sin\theta \cos\phi + \sin\alpha_n \sin\theta \sin\phi]} \tag{2}$$

where N is the number of elements, I_n and ϕ_n are the excitation amplitude and phase for the nth element, k is the wavenumber, r_n and α_n are the radius and angle of the nth element, and θ and ϕ are polar coordinates. In a uniform circular antenna array, $\alpha_n = 2n\pi/N$, and in order to generate OAM modes, $\phi_n = n\Delta\phi = 2n\pi/N$. The radiation pattern

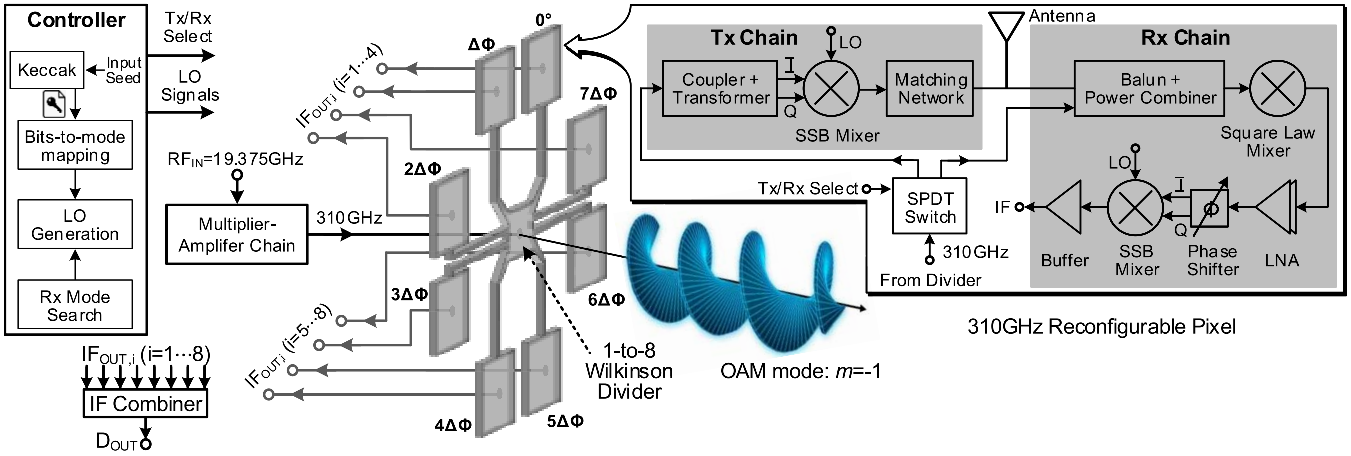

Fig. 2. Architecture of the 0.31-THz-OAM transceiver in CMOS.

of the antenna array is determined by multiplying AF with the simulated radiation pattern of the patch antenna. This method is adopted to optimize the array diameter with sidelobe suppression with a fixed number of antennas.

To generate a pure OAM state, in theory, the largest OAM mode can be $|m| < N/2$. In this design, $N = 8$, and seven OAM modes ($\phi = 2m\pi$ and $m = 0, \pm1, \pm2, \pm3$) can be generated. However, in this chip work, we demonstrate only the $m = 0, +1, -1$, and ±1 modes. The intensity and phase profiles generated by the circular patch antenna array are simulated in the full-wave EM simulator, HFSS [33], for the four OAM modes. The far-field distributions of intensity and phase over a non-model plane are recorded in Fig. 3. In Fig. 3(a), it can be seen that, for $m = 0$, the radiated power is centered at the beam axis, while, for $m = +1$ and -1, the same radiated power is now uniformly distributed around the central null running along the beam axis. For the superposed mode $m = (+1) + (-1)$, there are two counter-rotating beams with a null separating them along the diagonal. Fig. 3(b) shows that left- and right-handed phases twist for $m = +1$ and -1, respectively, along with the phase singularity at the center. The plane wave has no phase variation, and the superposed mode shows two out of phase rotations. Note that the phase distribution is not discontinued for superposed mode; rather, it represents an intensity null along the diagonal.

The simulated radiation pattern of the antenna array is shown in Fig. 4. For the $m = +1$ mode, a sharp fall in the array directivity at the center is observed due to phase singularity. Note that it has a single donut-shaped lobe with a null in the center rather than two separate sidelobes. The sidelobes are ~20 dB lower than the main beam for the array with a diameter of one wavelength λ in air. The radiation patterns for the antenna array with the diameters of 1.25λ and 1.5λ are also shown in the inset of Fig. 4, and their sidelobes are only ~10 dB lower than the main beam. This is undesired because it makes the transmission more prone to eavesdropping. Therefore, a diameter of λ for the circular array is adopted in this design.

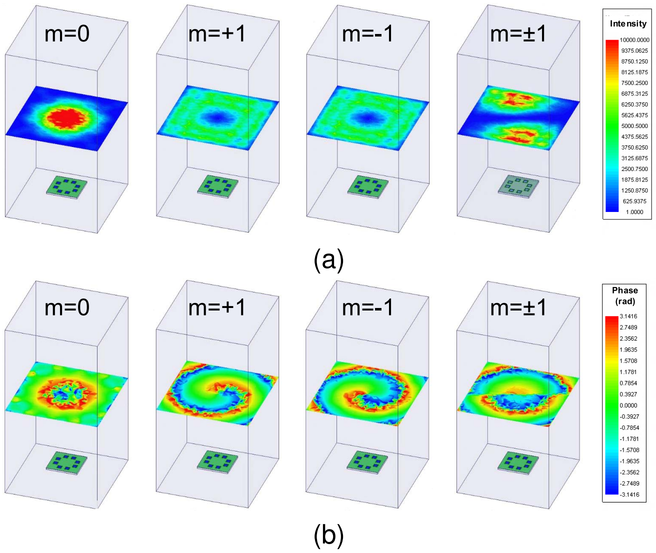

Fig. 3. Simulated (a) intensity and (b) phase distributions for four OAM modes from a 310-GHz circular patch antenna array.

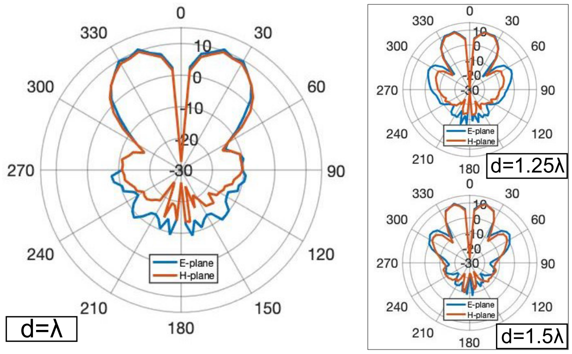

Fig. 4. Simulated directivity for the circular antenna array with a diameter of λ for $m = +1$. The inset shows the radiation patterns for the diameters of 1.25λ and 1.5λ.

One major challenge of this antenna array is the distribution of the 310-GHz signal to all the Tx and Rx chains with the exact same amplitude and phase, which is required to maintain the fidelity of OAM modes. To this end, a modular design is adopted for the antenna array, where it is divided into four quadrants with two pixels in each, as shown in Fig. 5. The 310-GHz signal is divided into eights pixel through a symmetric 1-to-8 Wilkinson power divider. The limited space requires

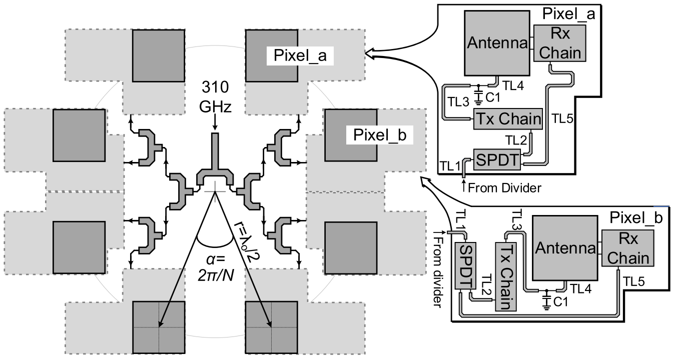

Fig. 5. Floor plan of circular antenna array showing phase-coherent distribution of the 310-GHz signal to all the pixels. The arrangement of circuit blocks in the two pixels with matching networks is also shown, which avoids phase mismatch at the Tx antenna and the Rx mixer.

the floor plan of two pixels in one quadrant to be different (see Pixel_a and Pixel_b in Fig. 5). The matching networks between different circuits are designed to have identical phase shifts. This is done by folding some transmission lines to match both the pixels. In simulations, the amplitude and phase mismatches are negligible between the pixels. The distribution of 8-MHz LOs (from the controller to each pixel) also follows the same path though the phase coherence requirement, in this case, is much relaxed. The power divider has a simulated insertion loss of 0.8 dB and is implemented using 2-μm-wide M9 metal traces.

B. Dual-Feed Patch Antenna

To enable front-side radiation, each pixel integrates a patch antenna that is shared between the Tx and Rx chains. To realize such sharing, a square shape patch with two feeds is adopted so that both feeds excite the same mode (TM_{100} in this case) and have the same resonance frequency (∼310 GHz) [34]. As indicated in Fig. 6(a), to excite the TM_{100} mode, we can either use a differential feed symmetrically connected to the patch edge along the x-direction or a single-ended feed connected to the center of the patch edge along the y-direction. Accordingly, the Tx chain has a single-ended output, and the Rx chain has a differential input. This scheme ensures that both Tx and Rx have the same linear polarization and helps in avoiding phase ambiguity from the wavefront twist. When the chip is working in the Tx mode, both Tx and Rx ports are matched, and this leads to Tx–Rx coupling, as shown in Fig. 6(b), causing ∼2-dB loss in the radiated power. In the Rx mode, the Tx chain presents a high impedance to the antenna as its mixer is turned off, and the Rx–Tx coupling is less, as shown in Fig. 6(c) with ∼1.3 dB loss in the received power. In future iterations, a patch antenna with two orthogonal single-ended feeds can be adopted that excites TM_{100} and TM_{010} modes in Tx and Rx modes, respectively, to mitigate Tx–Rx coupling.

Regarding the implementation of the patch antenna, its radiator uses the top aluminum (Al-pad) layer of the CMOS process and has a dimension of 218×218 μm^2. The ground plane of the antenna is made out of the M1 and M2 layers (∼8-μm below the radiator), and there is no dummy metal filling between the radiator and the ground. The antenna is also enclosed by a ground wall (M1-to-Al pad stack), which is 20-μm away from the patch on all sides. It reduces the coupling with neighboring electronics and antennas while having a negligible impact on the antenna performance. The square shape of the antenna also has a negligible impact on its performance. The peak directivity and radiation efficiency of the antenna in the HFSS simulation are 5 dBi and 37%, respectively. The antenna array has a peak directivity of 11 dBi for the plane wave mode with the same radiation efficiency.

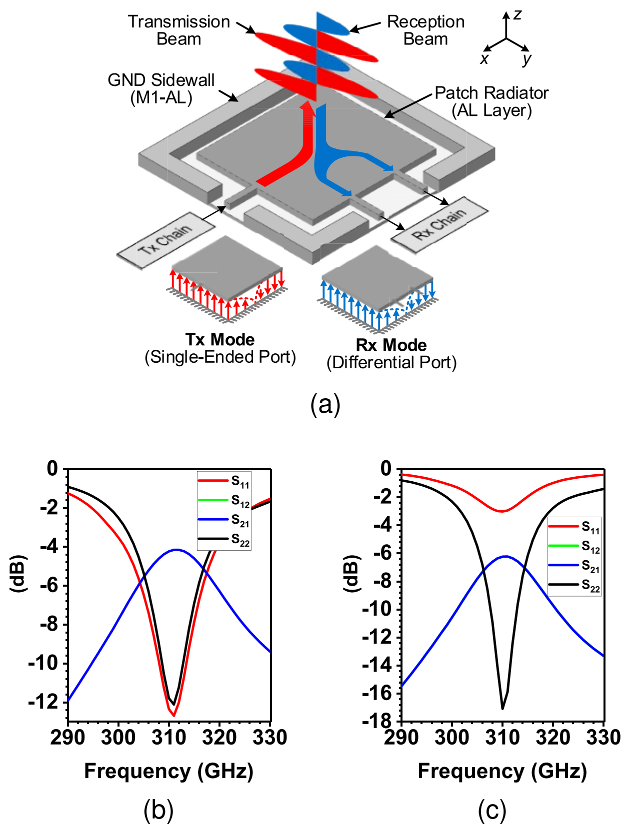

Fig. 6. (a) Schematic of multi-port patch antenna with the same excited mode (TM_{100}) for both Tx and Rx. Simulated s-parameters when (b) both Tx and Rx ports are matched, and (c) Tx presents high impedance, and the Rx port is matched.

III. DESIGN OF THE 310-GHz RECONFIGURABLE PIXEL

The block diagram of the THz-OAM pixel is shown in the inset of Fig. 2. The Tx/Rx mode selection is realized by a coupled-line-based SPDT switch [see Fig. 7(a)] [35], which directs the 310-GHz input to either Tx or Rx chain. As shown in Fig. 7(b), the simulated insertion loss (S_{21}) and isolation (S_{31}) of the switch, when EN = 1, are 3.8 and 15 dB, respectively. The coupled transmission lines are 40-μm long and are implemented on M9 with 5-μm width and 2-μm spacing. A capacitor $C_1 \approx 19$ fF is required for input matching, whereas the parasitic capacitances from the 24-μm/60-nm NMOS devices (M_1 and M_2) are included in the output matching. MOSFETs in the 65-nm bulk CMOS process have poor switching performance at THz frequencies; although wider channel provides smaller ON-resistance, there is also stronger coupling of THz signal from the channel to the LO wire through the gate-channel capacitance. To block

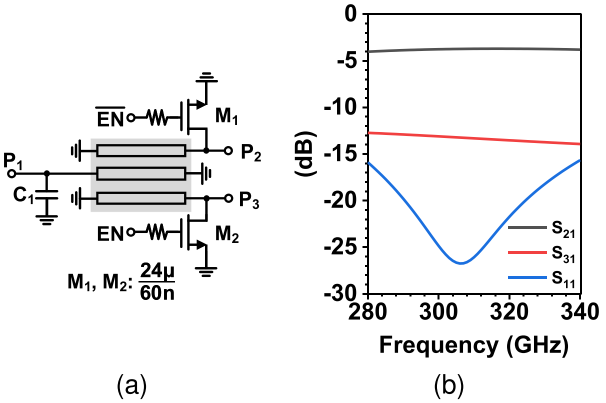

Fig. 7. (a) Schematic of coupled-line-based SPDT switch. (b) Simulated insertion loss (S_{21}), isolation (S_{31}), and return loss (S_{11}) for the SPDT switch with EN = 1.

such coupling, a set of 8-kΩ resistors are added in series with the transistor gates, which improves the switch insertion loss.

A. Design of the THz-OAM Transmitter Chain

The Tx chain consists of a coupler and a transformer for generating quadrature 310-GHz signals, followed by a single-sideband (SSB) mixer and an antenna matching network, as shown in Fig. 8(a). Compared to conventional high-frequency phase shifters, our mixer-based scheme offers precise phase control and phase-independent amplitude response, which are critical to the fidelity of the OAM wavefront. Although a double-sideband (DSB) mixer involves simpler hardware implementation, we note that the generated upper and lower sidebands are applied with opposite phases from the LO; in our OAM transceiver, therefore, their associated beams would have opposite OAM modes that are undesired. In our design, an SSB mixer based on passive quad switches is adapted to not only suppress the upper sideband of the output but also to minimize the power consumption. The 8-MHz quadrature LO signals of the mixer are from a divide-by-4 static frequency divider dividing controller clock frequency. Although a divide-by-2 operation can also provide the 8-MHz quadrature LO signal, the additional availability of the LO phases (e.g., 45°, 135°, 225°, and 315°) provided in our divide-by-4 scheme is essential to generate the OAM modes. The phases of the RF and LO signals of the MOSFETs are arranged in the way that, at the central current-summing node, the lower sidebands of all branches add up constructively, while the upper sidebands cancel. Through the selection of LO phases, the controller changes the THz output phase. Different OAM modes can then be generated from the array. Mode switching is realized by the data-driven selection of the LO phases. The mode switching speed, although limited by the LO frequency, is sufficient for the transmission of a secret key (typically 256 bits).

The coupler is implemented on the M8 layer with 2.5-μm width and 2-μm spacing. The simulated insertion loss, and amplitude and phase mismatches of the coupler are 0.5 dB, 0.1 dB, and 0.8°, respectively, as shown in Fig. 8(b). The single-loop center-tap transformer is implemented on the M9 layer with 3-μm width and 3-μm spacing. The simulated insertion loss, and amplitude and phase mismatches of the transformer are 1.3 dB, 0.1 dB, and 0.3°, respectively, as shown in Fig. 8(c). In Fig. 8(d), we show the EM-circuit co-simulation results of the entire Tx chain. An overall conversion loss of 14 dB is achieved at $f_{\mathrm{RF}} = 310$ GHz, at the expense of zero static dc power. The module also effectively suppresses the components at $f_{\mathrm{RF}} + f_{\mathrm{LO}}$ and $f_{\mathrm{RF}} \pm 2f_{\mathrm{LO}}$. The component at $f_{\mathrm{RF}} + 3f_{\mathrm{LO}}$, due to its constructive summation at the mixer output node, appears at the output spectrum, with the 10-dB rejection ratio. This component is $4f_{\mathrm{LO}}$ away from the required f_{RF}-f_{LO} component and is filtered at the IF output of the Rx. In the future, this may be improved by adopting a polyphase N-path mixer structure.

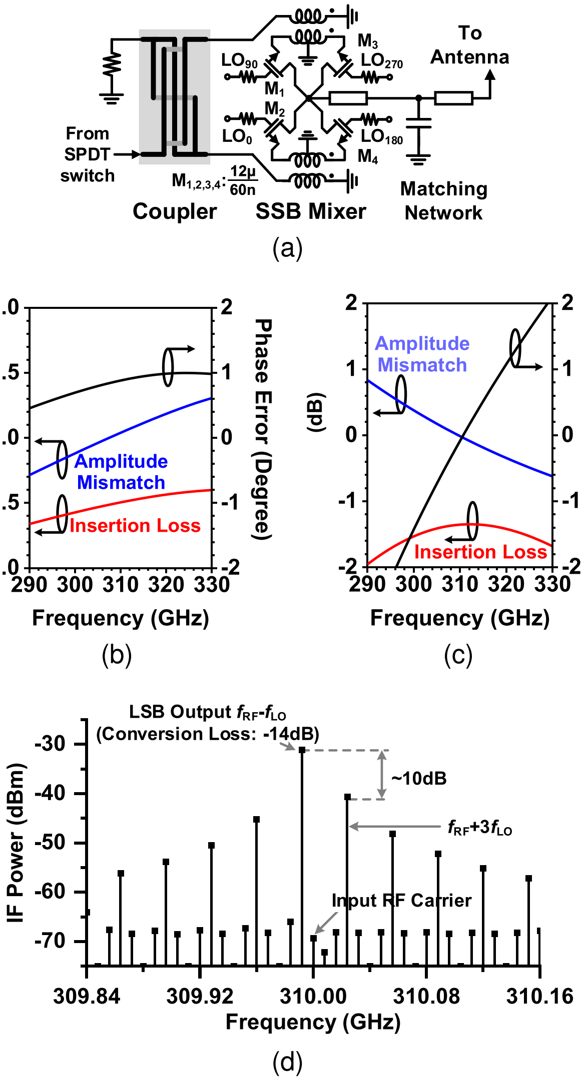

Fig. 8. (a) Schematic for Tx chain including coupler, transformers, SSB mixer, and matching network. (b) Simulated insertion loss and output mismatch of the coupler. (c) Simulated insertion loss and output mismatch of the transformer. (d) Simulated output spectrum of the Tx chain with a −16-dBm RF input ($f_{\mathrm{RF}} = 310$ GHz) and quadrature LO signals at $f_{\mathrm{LO}} = 8$ MHz.

B. Design of the THz-OAM Receiver Chain

The schematic for the Rx chain is shown in Fig. 9(a). For chip compactness, the receiver mode uses the same

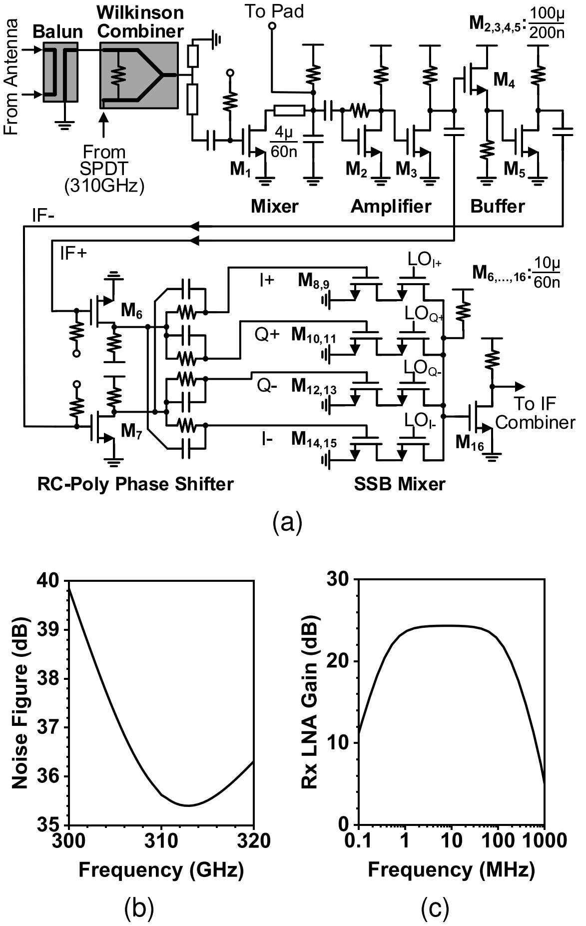

Fig. 9. (a) Schematic for the Rx chain. (b) Simulated receiver NF. (c) Simulated gain of the baseband amplifier.

antenna, where the input wave is extracted through differential feeds along with the antenna H-plane [see Fig. 6(a)]. Since the operation frequency of our transceiver has exceeded the transistor speed limit of the 65-nm CMOS process used here ($f_{\max} \approx 280$ GHz), a pre-amplifier in the RX front end would not be possible. Hence, an active-mixer-first architecture is adopted. A balun converts the differential received signal to a single-ended signal, which combines with the SPDT-directed 310-GHz signal in a Wilkinson combiner. The 310-GHz signal now behaves as a THz LO that down-converts the received signal inside a MOSFET-based square-law mixer. The generated IF signal, carrying the same phase as the local input wave, is then amplified and undergoes a phase-shifting process inside an SSB mixer (for the same reason as that in the transmission mode). When such a phase shift compensates for the OAM phase gradient $\Delta\phi$ among the THz pixels, all IF outputs become in-phase. The IF combiner in Fig. 2 then adds them constructively and provides $\mathrm{D_{OUT}}$ as an indicator of whether the incident wave matches the currently selected OAM mode. For simultaneous detection of multiple OAM modes, the pixel IF signals can be directly extracted through pads, and amplified and digitized using ADC. Then, relative phase shifts can be determined by digital processing.

A return-path-gap (RPG)-based balun similar to the one presented in [36] is used. It consists of two microstrip lines coupled via a slot in the ground plane (i.e., RPG). The RPG slot, closed by four quarter-wavelength slot resonators in the ground plane, only allows transmission (hence, input–output coupling) of the quasi-TE-mode wave, which is excited by a differential signal in the input microstrip lines. The simulated insertion loss for the differential mode is $\sim$1 dB. The balun is implemented using 2-μm-wide M9 microstrip lines and slots in a shunted M1–M3 ground. The mixer is based on an NMOS device (4-μm/60-nm) with drain bias and sub-threshold gate bias ($V_G = 0.3\ \mathrm{V} < V_{\mathrm{th}}$). This topology yields lower conversion loss as compared to a passive mixer (without drain bias) but degrades the noise figure (NF) due to flicker noise [37]. Therefore, an *R–C* high-pass filter is added between the mixer and baseband amplifier to suppress the low-frequency noise. In the simulation, the mixer has input $P_{1\,\mathrm{dB}}$ of -5.2 dBm, which is much higher than the LO power (~ -16 dBm). The non-linear downconversion process is highly dependent on LO power, and low LO power (due to distribution of LO from one active path) gives higher conversion loss. As a result, in the simulation, the SSB NF of the receiver is 36 dB at 310 GHz [see Fig. 9(b)]. Following the mixer is a two-stage, self-biasing baseband amplifier, which has 3.2-nV/Hz$^{1/2}$ simulated input-referred noise (lower than the mixer output noise), enables an overall conversion gain of 24 dB for the receiver chain [see Fig. 9(c)]. To generate the IF I-Q signals for the SSB mixer, a set of broadband and compact *R–C* polyphase filters (PPFs) are adopted. The SSB mixer uses the same LO signals that are employed in the Tx chain. In the simulation, the SSB, including the *R–C* PPF, has a conversion loss of 12 dB.

IV. 310-GHz MULTIPLIER-AMPLIFIER CHAIN

The 310-GHz multiplier-amplifier signal source is shown in Fig. 10 (a similar design is reported earlier in [38]). At the input of the frequency conversion daisy chain, two push–push frequency doublers that are cascaded through a transformer are used to convert the input signal at 19.375 GHz to 77.5 GHz, as shown in Fig. 11(a). In simulation, the conversion gain of two doublers is -6.8 dB [see Fig. 11(b)], and the output power after the buffer is $\sim$5 dBm [see Fig. 11(c)]. The schematic of Doubler 1 is shown in Fig. 12. The millimeter-wave signal from the frequency conversion chain drives a common-source buffer (M_1) and is then turned into differential mode through a single-loop transformer ($\mathrm{TF_1}$). A push–push structure is then used to generate the second-harmonic component while suppressing the tone at the input frequency. As shown in Fig. 12(b) and (c), the peak conversion gain and output power of Doubler 1 are -3.4 and 1.5 dBm, respectively. The simulated dc power of the entire circuit in Fig. 12 is 21 mW.

As shown in Fig. 10, before the second frequency-doubling, the signal from Doubler 1 is converted to differential mode using a balun and is boosted by a chain of amplifiers [see Fig. 13(a)]. Since the amplifiers are based on a pseudo-differential topology with a neutralization technique (details to be given next), they are sensitive to any amplitude and phase imbalance of the input signal. To minimize such imbalance, a sub-THz balun structure based on a pair of folded

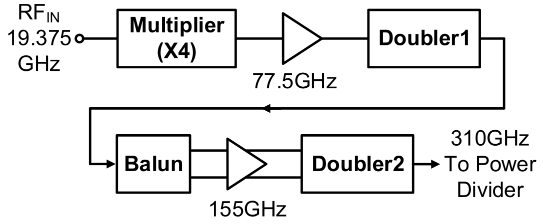

Fig. 10. Block diagram of the 310-GHz multiplier-amplifier signal source.

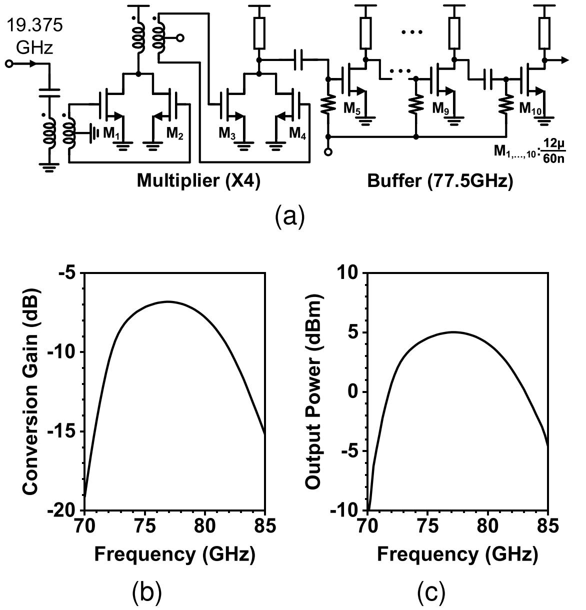

Fig. 11. (a) Schematic of the input multiplier (×4) and buffer. (b) Simulated conversion loss of the input multiplier with $P_{\text{in}} = 6$ dBm. (c) Simulated output power of the buffer.

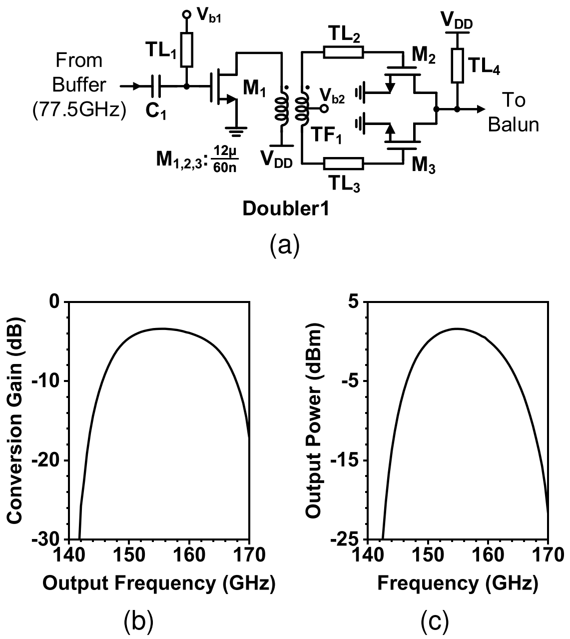

Fig. 12. (a) Schematic of Doubler 1. (b) Simulated doubler conversion gain at varying output frequency (the input power variation from the preceding circuitry is also included). (c) Simulated doubler output power.

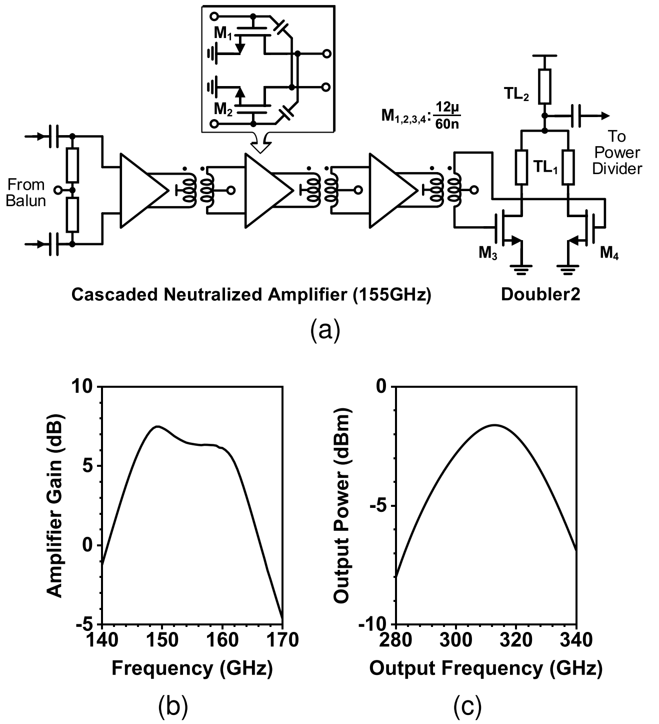

Fig. 13. (a) Schematic of Doubler 2 and its input amplifier. (b) Simulated gain of the cascaded neutralized amplifier chain (the input power variation from the preceding circuitry is also included). (c) Simulated output power of Doubler 2 with an input power of +5 dBm.

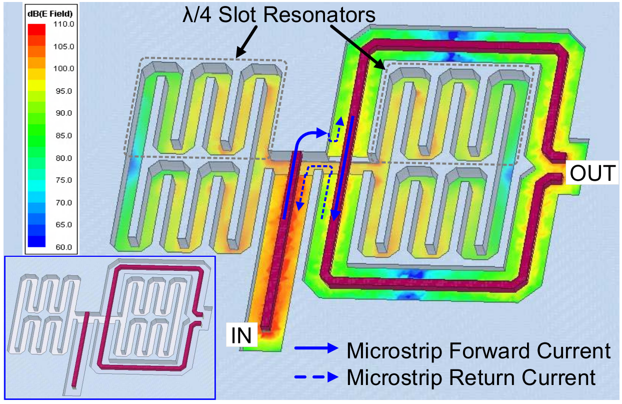

Fig. 14. Simulated electric-field distribution of the 155-GHz slot-based balun with the 3-D structure shown in inset.

slot resonators [39] is adopted. As shown in Fig. 14, the balun input and output consist of a single-ended microstrip line and a pair of differential microstrip lines, respectively. A gap in the ground plane couples the input and output; it is also enclosed by two pairs of quarter-wavelength slot resonators that present high impedance on the two ends of the ground gap. The resonators are folded for compact size and minimum radiative loss. Full-wave EM simulation shows that the insertion loss of the balun is 1.3 dB, and the amplitude/phase imbalance is negligible.

The signal generated by the slot balun is then amplified by three identical, pseudo-differential amplifier stages, shown in Fig. 13(a). The stages are coupled through central-tapped transformers. In each stage, a cross-coupled capacitor pair is used to create negative capacitance that cancels the C_{gd} of the transistors. Although this neutralization scheme does not

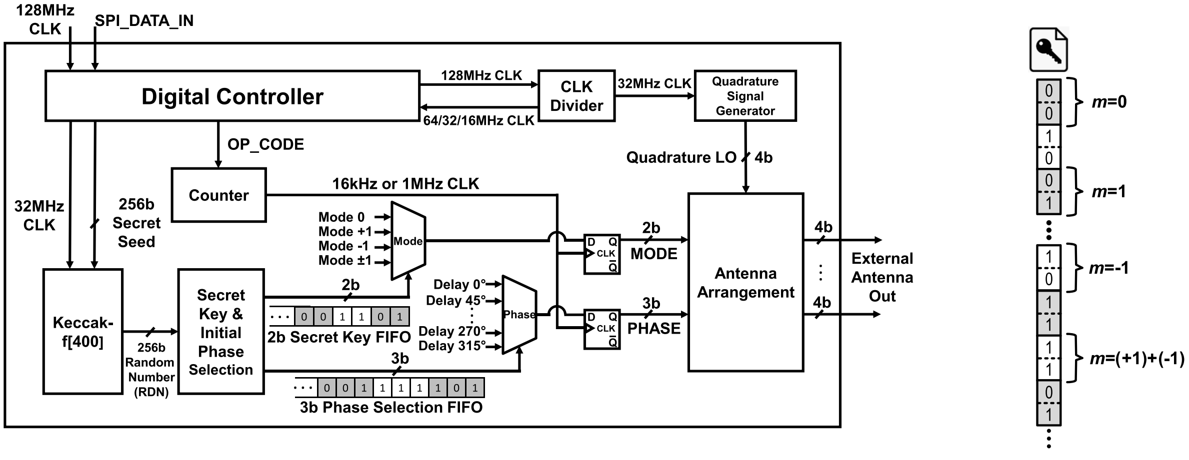

(a) (b)

Fig. 15. (a) Controller architecture for pseudorandom key generation and OAM modulation. (b) Mapping between the bits of secret key and the OAM modes.

provide the highest possible gain, the device unilaterization that this scheme enables allows for higher stability and broader bandwidth. The simulated gain of the amplifier chain is shown in Fig. 13(b), with an average value of ~7 dB in the 150 ~ 160-GHz band. Finally, the signal is frequency-doubled again by a pair of push–push transistors (M_3 and M_4). The common node of TL_1 is virtual ground for the differential 155-GHz signals, whereas it is matched to output for the in-phase 310-GHz signals. The inductive reactances provided by transmission lines TL_1 (slightly shorter than $\lambda/4$) resonate with the parasitic capacitances of the NMOS devices at 155 GHz. This boosts the swing of the device drain voltages (hence, higher device non-linearity). TL_2 is used as part of the output matching network and helps in extracting the 310-GHz signal through a dc isolation capacitor. In the simulation, the amplifier chain and Doubler 2 consume dc power of 57 and 24.8 mW, respectively, and the final TX output power [as shown in Fig. 13(c)] is ~ -1.6 dBm at 310 GHz.

V. CONTROLLER AND OAM MODE MAPPING

The system-level architecture of the pseudorandom key generation and the OAM modulation controller is shown in Fig. 15(a). The high-level protocol flow is given as follows.

1) A secret seed for key generation and an opcode are transferred into the chip through SPI. The controller operates with a global clock of 128-MHz frequency and divides it into different local clocks of 16, 32, and 64 MHz.
2) Keccak-f[400] takes a 256-bits secret seed and generates a 256-bits pseudorandom number, which is converted into a secret key and phase selection bits. Each 2 bit of the secret key corresponds to one OAM mode, while each 3 bit of phase selection corresponds to one initial phase distribution. The frequency of OAM modulation achieves up to 1 MHz, while the Keccak operates with the 32-MHz clock.
3) A quadrature LO is generated from the local clock, and the antenna arrangement block changes the THz output phase, generating different OAM modes from the antenna array based on the current mode and the phase distribution selection. The LO frequency is programmable between 16 kHz and 32 MHz with a nominal value of 8 MHz.

A. OAM Mode and Phase Selection Algorithm

Fig. 15(b) shows how the key is mapped to OAM modes. Every 2 bit (00, 01, 10, and 11) represents different OAM modes ($m = 0, +1, -1$, and ± 1). In order to increase the security of the modulation scheme, eight different phase patterns (with 45° difference) are randomly assigned to each mode. In the superposed mode ($m = \pm 1$), there exists a low-power area (null) due to the out-of-phase beams. By randomly switching between initial phases and hence different phase patterns, ambiguity increases manifold for eavesdroppers. However, random initial phases would not affect the reception by a legitimate receiver aligned to the beam axis.

B. Pseudorandom Number Generation

Keccak-f[400] [40] is an SHA3 cryptographic core and is used for pseudorandom number generation. The Keccak algorithm, commonly referred to as a sponge construction, supports two operations: absorb and squeeze. The Keccak state can be divided into rate and capacity components with the former determining throughput while the latter determining the security level. Keccak-f[400] implementation is used from [41], which uses a 400-bit internal state. The rate and capacity sizes are set to 128 and 272 bits, respectively.

In order to represent a 128-bit secret key, it requires a 64-long (128-bit/2-bit) OAM mode sequence. Each mode has eight different phase patterns ($45 \times m$ of phase change, and $m = 0, \ldots, 7$) so that another 192-bits (64×3-bits) random sequence is mandatory. The Keccak-f[400] block is exploited as a source of raw entropy to generate random bits at a clock frequency of 32 MHz. However, Keccak could only produce 256 bits, while we require 320 (128 bits for secret key and 192 bits for random phase pattern) random bits. Thus, we assigned the first 128-bit secret key. Then, the first 196 bits

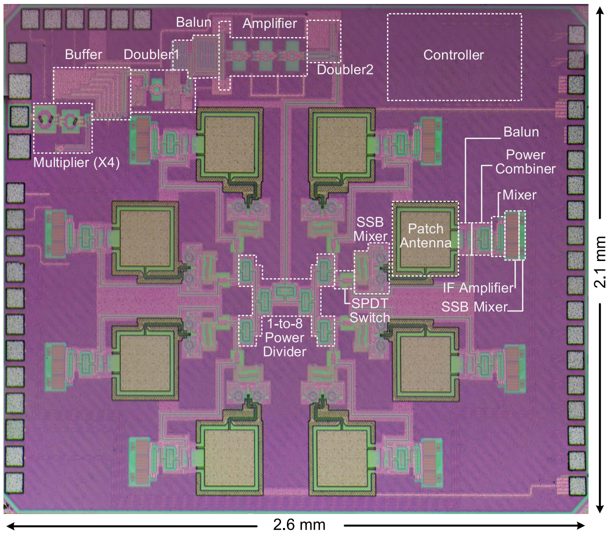

Fig. 16. Die photograph of the 310-GHz OAM CMOS chip.

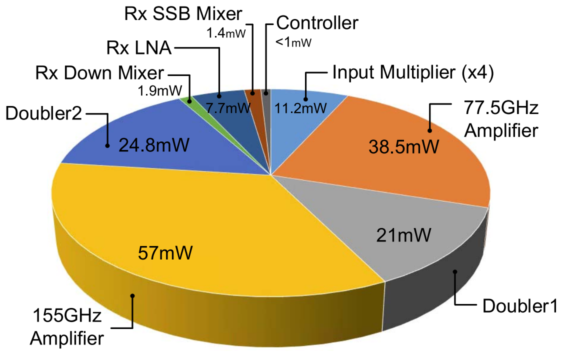

Fig. 17. Breakdown of the measured power consumption of the chip.

(most significant (MSB) 196 bits) are XORed with the next 196 bits (least significant (LSB) 196 bits) to generate phase pattern selection bits.

VI. EXPERIMENTAL RESULTS

The THz-OAM transceiver is fabricated in a TSMC 65-nm bulk CMOS process, and its die photograph is shown in Fig. 16. The chip occupies an area of 2.1×2.6 mm^2. The measured total dc power consumption by the chip is 154 and 166 mW in the Tx and Rx modes, respectively. The breakdown of power consumption of different components is shown in Fig. 17.

A. Characterization of Transmitter Mode

The measurement setup for the characterization of the Tx mode of the chip is shown in Fig. 18(a). Given the relatively large divergence of the OAM beam (due to the central null), a detachable low-cost TPX polymethylpentene lens (diameter = 25.4 mm and focal length = 10 mm) is placed at the front side of the chip to collimate the beam [see Fig. 18(b)]. The lens has a measured gain of ~20 dB. An SPP is used to convert a plane wave to OAM modes and vice versa, by introducing a linear phase variation along the azimuth direction. A custom-designed THz SPP is 3-D printed using polylactic acid (PLA) material, as shown in the inset of Fig. 18(b). The total height of SPP is given by the following equation:

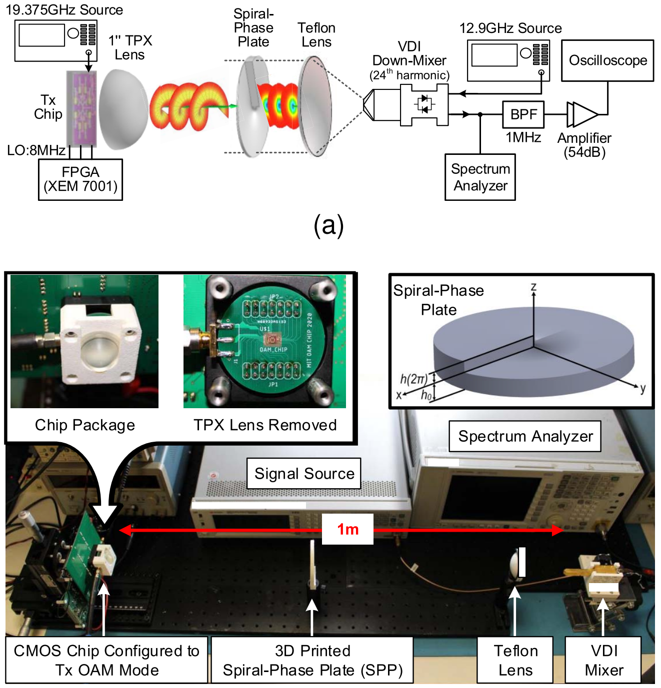

(a)

(b)

Fig. 18. (a) Diagram of the experimental setup for transmission mode characterization. (b) Photograph of the test setup. Rx is at a distance of 1 m from the transmitting chip, and an SPP is placed in between. The insets show the chip package with and without the lens and the structure of SPP.

$$h = h_o + h(\phi) = h_o + \frac{m\lambda\phi}{2\pi(n - n_o)} \tag{3}$$

where m is the OAM mode, λ is the wavelength in air, $\phi \in [0, 2\pi)$, and n is the refractive index. The relative dielectric constant of PLA obtained from the vendor's datasheet is 2.5, and hence, $n = 1.58$. This gives ramp height $h(2\pi)$ of 1.68 mm for $m = +1$ and -1 modes. The base height h_o is chosen to be 4.45 mm, which gives a measured loss of 12 dB.

First, the radiated power of the OAM array is measured by configuring the chip to generate a plane wave ($m = 0$ mode) and by placing a VDI WR-3.4 sub-harmonic mixer with an internal amplifier (combined conversion loss ~0 dB) and a feed horn 25 cm away. The corresponding EIRP is determined by the Friis equation [42] as

$$\text{EIRP} = P_{\text{IF}} + \text{CL}_M - G_R + 20\log\left(\frac{4\pi R^2}{\lambda}\right) \tag{4}$$

where P_{IF} is the measured IF signal power, CL_M is the conversion loss of the mixer, G_R is the feed horn gain (26 dBi), R is the distance between Tx and Rx, and λ is the wavelength. The peak measured EIRP of the chip is -4.8 dBm, as shown in Fig. 19. Next, the VDI receiver is mechanically scanned across a 2-D plane facing the chip in order to measure the wavefront intensity distribution of the chip output. The results in Fig. 20 show the expected null at the center of the $m = +1$ OAM mode. Our chip also enables and utilizes the superposition of the $m = +1$ and -1 modes, and the measured intensity plot in

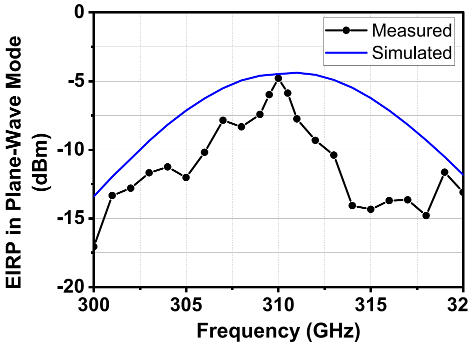

Fig. 19. Measured EIRP for plane wave mode ($m = 0$). Since the non-zero OAM modes have null in the center, EIRP is not well defined for such modes.

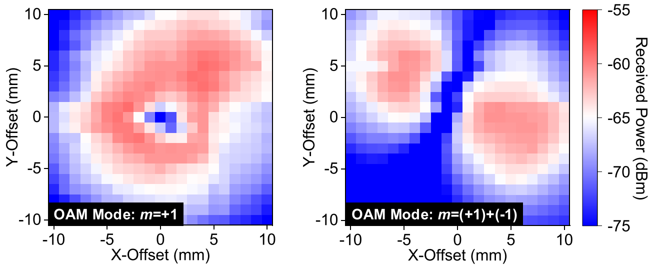

Fig. 20. Measured intensity distribution for OAM modes $m = +1$ and $m = (+1) + (-1)$ (superposition).

TABLE I
TX MODE CHECKING

Tx Mode	Rx SPP	P_{RX} (dBm)
0	No SPP	-50
0	+1	-69
0	-1	-70
+1	No SPP	-58
+1	+1	-64
+1	-1	-81
-1	No SPP	-58
-1	+1	-80
-1	-1	-64
±1	No SPP	-76
±1	+1	-68
±1	-1	-67

Fig. 20 presents the expected standing peaks and nulls as the result of the summation of the two counter-rotating wavefronts.

Direct measurement of phase spatial distribution is challenging due to the required μm-level Rx position precision at THz frequency; instead, the setup shown in Fig. 18 is adopted, where an SPP is placed in front of the VDI receiver and serves as "mode filter" by converting the input with the matched OAM mode into a plane wave. For different combinations between OAM modes of the transmitting array and the configuration of Rx SPP ($m = +1$ or -1), the VDI receiver output power is recorded in Table I. The measured spectra for the highlighted rows in Table I are shown in Fig. 21, showing a 17-dB difference between the matched and unmatched cases, indicating the purity of OAM modes generated by the chip. Note that, when the Rx has no SPP and when the Tx mode is non-zero, ideally, the Rx output power should be low, but any off-axis misalignment of the OAM array will get the Rx antenna to point at a non-zero portion of the OAM wavefront, resulting in non-negligible received power. It should also be noted that the P_{RX} values in the table include the SPP loss except for the "No SPP" case.

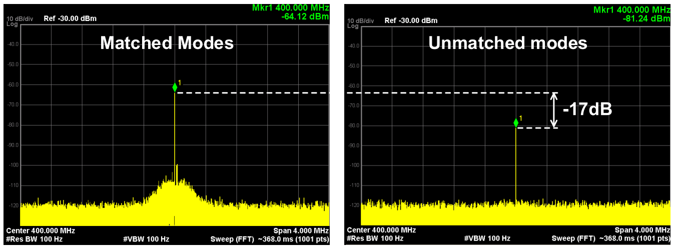

Fig. 21. Tx OAM mode-checking: a 17-dB difference in IF power is measured when the Tx mode is +1, and the Rx SPP is +1 (matched) and -1 (unmatched).

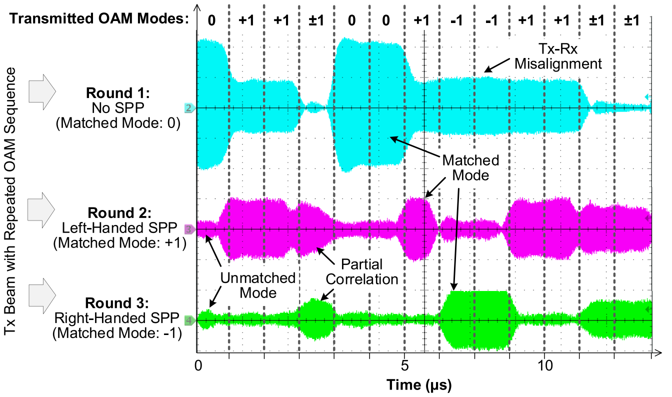

Fig. 22. Time-domain output of the receiver configured to respond to different OAM modes when it is illuminated by the same OAM sequence generated by on-chip Keccak.

In order to demonstrate the dynamic switching among OAM modes, the chip output mapped from a repeated 1-Mb/s Keccak-generated data sequence is verified, and the time-domain outputs of the Rx with different SPP configurations are shown in Fig. 22. It shows good correlation with matched modes, partial correlation of the $m = +1$ or $m = -1$ modes with the $m = (+1) + (-1)$ superposition mode, and the rejection of unmatched modes. Note that, in Rounds 2 and 3, the amplitude is lower than that in Round 1. This is due to the additional loss from the SPP. The presence of superposed mode with random initial phases increases the difficulty of eavesdropping by randomly posing intensity nulls to the eavesdropper, though at the expense of higher error probability for the legitimate receiver, as can be seen in Fig. 22. Note that the demonstrated 1-Mb/s data rate is for the intended application of transmission of the secret key and not the maximum achievable data rate of the proposed RF-frontend architecture.

B. Characterization of Receiver Mode

To test the reception mode of the chip, a VDI WR3.4 source ($P_{out} = -5$ dBm) is used. With an SPP inserted (see Fig. 23), the setup becomes an OAM mode generator. For different combinations between the configuration of Tx SPP ($m =$

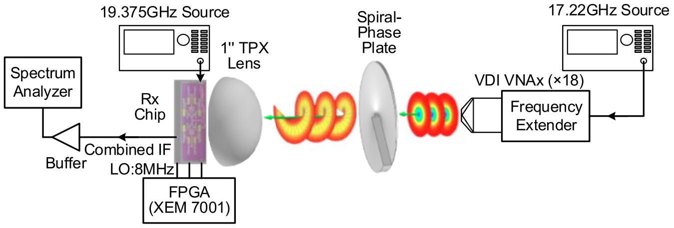

Fig. 23. Diagram of the experimental setup for receiver mode characterization.

TABLE II
Rx Mode Checking

Tx SPP	Rx Mode	P_{IF} (dBm)
No SPP	0	-64
No SPP	+1	-74
No SPP	-1	-75
No SPP	±1	-74
+1	0	-89
+1	+1	-78
+1	-1	-90
+1	±1	-84
-1	0	-91
-1	+1	-89
-1	-1	-78
-1	±1	-85

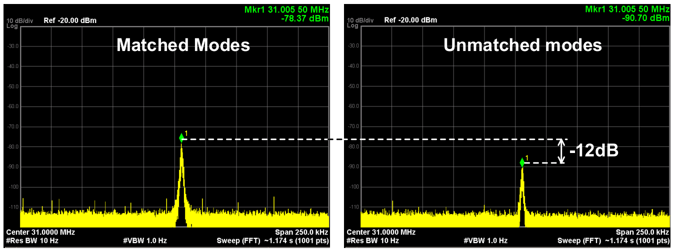

Fig. 24. Measured spectrum of combined IF in the Rx mode when Tx SPP is +1, and the Rx mode is +1 (matched) and −1 (unmatched).

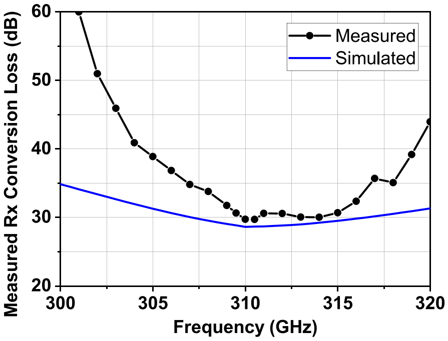

Fig. 25. Measured conversion loss of a single pixel for the plane wave mode ($m = 0$). The calculation assumes that the power incident to the chip is divided equally among the eight antennas.

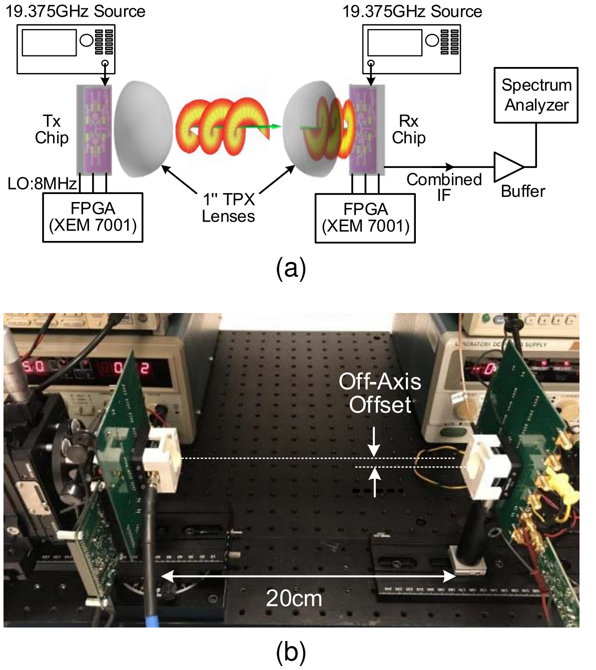

Fig. 26. (a) Diagram of the experimental setup for the characterization of full-silicon OAM link and sensitivity to co-axial alignment. (b) Photograph of the test setup.

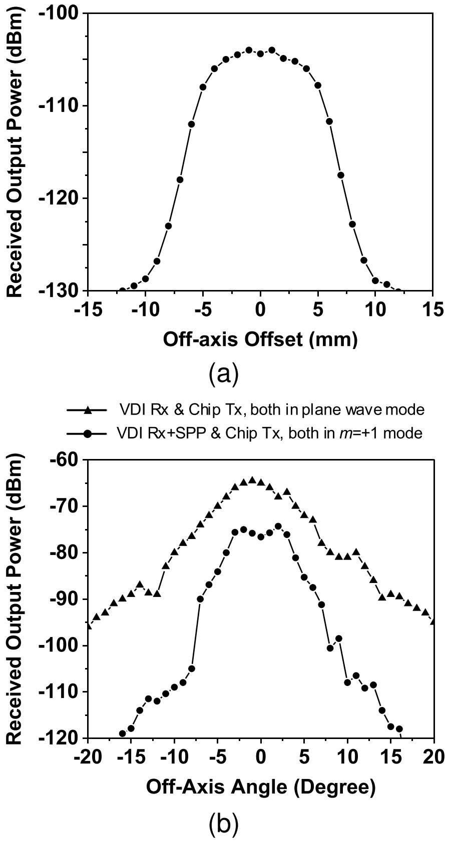

Fig. 27. (a) Measured sensitivity of OAM Tx–Rx to co-axial alignment. (b) Measured alignment angle sensitivity for the plane wave ($m = 0$) and OAM ($m = +1$) modes.

+1 or −1) and OAM modes of the receiving array, the combined IF power is recorded in Table II. The chip shows >10-dB rejection when the OAM modes on the two sides are unmatched for all combinations of the modes. One example is shown in Fig. 24, when the VDI Tx is always in $m = +1$ mode, whereas the chip detection mode is configured to $m = +1$ and $m = -1$, respectively, and the rejection is 12 dB. The measured conversion loss of the chip for the plane wave ($m = 0$) is ~30 dB, as shown in Fig. 25. The LO distribution network for the Rx chain seems shifted upward resulting in

TABLE III
COMPARISON WITH PRIOR RF AND mm-WAVE OAM PROTOTYPES

	Nature Comm. '14 [9]	**Wireless Comm. '17 [10]**	**ICCW '20 [11]**	**This work**
Implementation	Discrete Transceivers +SPP+Quasi-Optical Beam Combiner	Active-Driven Antenna Arrays+Parabolic Reflectors	Active-Driven Antenna Arrays	Active-Driven Antenna Array on a 65-nm CMOS Chip+Teflon Lens
Frequency (GHz)	28	10	40	310
OAM Modes	±1, ±3	±2, ±3	0, ±1, ±2, ±3	0, +1, -1, ±1
Data Modulation	16 QAM/Mode Dual Polarization	32 QAM on each mode, Full Duplex	256 QAM/Mode Dual Polarization	Bits-to-Mode OAM Hopping
Radiated Power (dBm)	8	0	11.5	-24.8 (-4.8 EIRP)
Antenna Aperture Diameter (cm)	30	60	120	1.35
Application	Enhanced Spectral Efficiency	Enhanced Spectral Efficiency	Enhanced Spectral Efficiency	Physical-Layer Security
DC Power (mW)	N/A	N/A	N/A	154 (Tx), 166 (Rx)

lower LO power input to the down-conversion mixer at the lower frequency end. This explains the discrepancy between the simulation and measurement results.

C. Characterization of CMOS OAM Link

Finally, a full-silicon OAM link is tested using the measurement setup shown in Fig. 26. Two chips configured in Tx and Rx modes, respectively, are placed 20 cm apart. Both the chips are configured to be in the $m = +1$ mode, and the combined IF output from the Rx chip is measured with controlled axial misalignment, as shown in Fig. 27(a). It is evident that the reception is highly sensitive to the Rx offset from the array axis demonstrating the aforementioned PLS. Note that the experiment is performed with the matched modes. Without prior knowledge of the mode (as for eavesdropper), the mode detection will be even harder with offset misalignment. The measured beam profiles (using the setup shown in Fig. 18), when both Tx chip and Rx SPP are in mode $m = 0$ and $+1$, are shown in Fig. 27(b). The result clearly shows that an OAM Tx–Rx link, compared to its plane-wave counterpart, has a much higher sensitivity to angular misalignment.

VII. CONCLUSION

A 0.31-THz uniform circular patch antenna array is demonstrated in the 65-nm CMOS process that can transmit and receive waves carrying OAM. The chip is capable of dynamically generating data-driven OAM modes: $m = 0, +1, -1$, and $(+1) + (-1)$, as well as detecting these modes with $>$10-dB rejection of mismatched modes. Table III provides a comparison with other discrete-component-based RF and mm-Wave OAM prototypes. Note that, in the compared works, each OAM mode is transmitting its own independent data stream, and multiple OAM modes are spatially multiplexed to enhance spectral efficiency. However, in our work, a single data stream is encoded in multiple OAM modes to transmit it securely. Our work is also the first demonstration of a full-silicon OAM link at any frequency and is the first hardware delivering dynamic OAM mode switching in the THz regime.

The presented work opens up opportunities in mode-multiplexing wireless communications and PLS for one-way key transmission using low-cost microelectronic chips. The chip can use OAM modes for transmitting security keys (usually 256 bits) at a relatively low data rate (limited by the SNR due to the central null) and then switch to the plane wave mode for exchanging symmetrically encrypted data at higher data rates. In future iterations, the 155-GHz power amplifier (PA) and the frequency doubler can be integrated inside the pixel. This will not only improve the link budget for high-speed wireless communication but also make the architecture more scalable for higher OAM modes. PA-integrated pixels placed in concentric circles and all driven by the same reference signals will make the generation and multiplexing of higher order OAM modes feasible. This will empower a wide range of new applications of OAM in the THz regime [43]–[45].

ACKNOWLEDGMENT

The authors thank Dr. Jenshan Lin at the National Science Foundation for his support of this project. They also acknowledge Prof. Yang Yang at the University of Technology Sydney for the 3-D printing of the spiral-phase plate (SPP) plates.

REFERENCES

[1] J. H. Poynting, "The wave motion of a revolving shaft, and a suggestion as to the angular momentum in a beam of circularly polarised light," *Proc. Roy. Soc. London A*, vol. 82, no. 557, pp. 560–567, Jun. 1909.

[2] R. A. Beth, "Direct detection of the angular momentum of light," *Phys. Rev.*, vol. 48, p. 471, Sep. 1935.

[3] R. A. Beth, "Mechanical detection and measurement of the angular momentum of light," *Phys. Rev.*, vol. 50, no. 2, pp. 115–125, Jul. 1936.

[4] V. Bazhenov, M. Vasnetsov, and M. Soskin, "Laser beams with screw dislocations in their wavefronts," *J. Exp. Theor. Phys.*, vol. 52, pp. 429–431, Oct. 1990.

[5] L. Allen, M. W. Beijersbergen, R. Spreeuw, and J. Woerdman, "Orbital angular momentum of light and the transformation of Laguerre–Gaussian laser modes," *Phys. Rev. A, Gen. Phys.*, vol. 45, no. 11, pp. 8185–8189, Jun. 1992.

[6] B. Thidé *et al.*, "Utilization of photon orbital angular momentum in the low-frequency radio domain," *Phys. Rev. Lett.*, vol. 99, no. 8, Aug. 2007, Art. no. 087701.

[7] F. Tamburini, E. Mari, B. Thidé, C. Barbieri, and F. Romanato, "Experimental verification of photon angular momentum and vorticity with radio techniques," *Appl. Phys. Lett.*, vol. 99, no. 20, 2011, Art. no. 204102.

[8] L. Allen, M. Padgett, and M. Babiker, *The Orbital Angular Momentum of Light* (Progress in Optics), vol. 39, E. Wolf, Ed. Amsterdam, The Netherlands: Elsevier, 1999, pp. 291–372.

[9] Y. Yan *et al.*, "High-capacity millimetre-wave communications with orbital angular momentum multiplexing," *Nature Commun.*, vol. 5, no. 1, Sep. 2014, Art. no. 4876.

[10] W. Zhang *et al.*, "Mode division multiplexing communication using microwave orbital angular momentum: An experimental study," *IEEE Trans. Wireless Commun.*, vol. 16, no. 2, pp. 1308–1318, Feb. 2017.

[11] H. Sasaki, Y. Yagi, T. Yamada, T. Semoto, and D. Lee, "An experimental demonstration of over 100 Gbit/s OAM multiplexing transmission at a distance of 100 m on 40 GHz band," in *Proc. IEEE Int. Conf. Commun. Workshops (ICC Workshops)*, Jun. 2020, pp. 1–6.

[12] W. Cheng, W. Zhang, H. Jing, S. Gao, and H. Zhang, "Orbital angular momentum for wireless communications," *IEEE Wireless Commun.*, vol. 26, no. 1, pp. 100–107, Feb. 2019.

[13] O. Edfors and A. J. Johansson, "Is orbital angular momentum (OAM) based radio communication an unexploited area?" *IEEE Trans. Antennas Propag.*, vol. 60, no. 2, pp. 1126–1131, Feb. 2012.

[14] S. Dang, O. Amin, B. Shihada, and M.-S. Alouini, "What should 6G be?" *Nature Electron.*, vol. 3, no. 1, pp. 20–29, Jan. 2020.

[15] T. S. Rappaport *et al.*, "Wireless communications and applications above 100 GHz: Opportunities and challenges for 6G and beyond," *IEEE Access*, vol. 7, pp. 78729–78757, 2019.

[16] M. Polese, J. M. Jornet, T. Melodia, and M. Zorzi, "Toward end-to-end, full-stack 6G terahertz networks," *IEEE Commun. Mag.*, vol. 58, no. 11, pp. 48–54, Nov. 2020.

[17] V. Petrov, T. Kurner, and I. Hosako, "IEEE 802.15.3d: First standardization efforts for sub-terahertz band communications toward 6G," *IEEE Commun. Mag.*, vol. 58, no. 11, pp. 28–33, Nov. 2020.

[18] (2019). *Federal Communication Commission (FCC) Takes Steps to Open Spectrum Horizons for New Services and Technologies*. [Online]. Available: https://docs.fcc.gov/public/attachments/DOC-356588A1.pdf

[19] H. V. Poor and R. F. Schaefer, "Wireless physical layer security," *Proc. Nat. Acad. Sci. USA*, vol. 114, no. 1, pp. 19–26, Jan. 2017.

[20] J. Ma *et al.*, "Security and eavesdropping in terahertz wireless links," *Nature*, vol. 563, no. 7729, pp. 89–93, Nov. 2018.

[21] W. Huang, Y. Li, D. Wei, and Q. Zhang, "Research on physical layer security scheme based on OAM," in *Proc. Int. Conf. Wireless Algorithms, Syst., Appl.*, vol. 11604, Jun. 2019, pp. 573–586.

[22] I. B. Djordjevic, "OAM-based hybrid free-space optical-terahertz multidimensional coded modulation and physical-layer security," *IEEE Photon. J.*, vol. 9, no. 4, Aug. 2017, Art. no. 7905812.

[23] A. Babakhani, D. B. Rutledge, and A. Hajimiri, "Transmitter architectures based on near-field direct antenna modulation," *IEEE J. Solid-State Circuits*, vol. 43, no. 12, pp. 2674–2692, Dec. 2008.

[24] J. Guo, L. Poli, M. A. Hannan, P. Rocca, S. Yang, and A. Massa, "Time-modulated arrays for physical layer secure communications: Optimization-based synthesis and experimental assessment," *IEEE Trans. Antennas Propag.*, vol. 66, no. 12, pp. 6939–6949, Dec. 2018.

[25] Q. Zhu, S. Yang, R. Yao, and Z. Nie, "Directional modulation based on 4-D antenna arrays," *IEEE Trans. Antennas Propag.*, vol. 62, no. 2, pp. 621–628, Feb. 2014.

[26] X. Lu, S. Venkatesh, B. Tang, and K. Sengupta, "4.6 space-time modulated 71-to-76 GHz mm-wave transmitter array for physically secure directional wireless links," in *IEEE ISSCC Dig. Tech. Papers*, Feb. 2020, pp. 86–88.

[27] A. M. Yao and M. J. Padgett, "Orbital angular momentum: Origins, behavior and applications," *Adv. Opt. Photon.*, vol. 3, no. 3, pp. 161–204, Jun. 2011.

[28] L. Cheng, W. Hong, and Z.-C. Hao, "Generation of electromagnetic waves with arbitrary orbital angular momentum modes," *Sci. Rep.*, vol. 4, no. 1, 2014, Art. no. 4814.

[29] A. Beniss, R. Niemiec, C. Brousseau, K. Mahdjoubi, and O. Emile, "Flat plate for OAM generation in the millimeter band," in *Proc. Eur. Conf. Antennas Propag. (EuCAP)*, 2013, pp. 3203–3207.

[30] K. Liu *et al.*, "Generation of OAM beams using phased array in the microwave band," *IEEE Trans. Antennas Propag.*, vol. 64, no. 9, pp. 3850–3857, Sep. 2016.

[31] S. Yu, L. Li, G. Shi, C. Zhu, X. Zhou, and Y. Shi, "Design, fabrication, and measurement of reflective metasurface for orbital angular momentum vortex wave in radio frequency domain," *Appl. Phys. Lett.*, vol. 108, no. 12, Mar. 2016, Art. no. 121903.

[32] M. I. W. Khan *et al.*, "A 0.31 THz CMOS uniform circular antenna array enabling generation/detection of waves with orbital-angular momentum," in *Proc. IEEE Radio Freq. Integr. Circuits Symp. (RFIC)*, Feb. 2021, pp. 203–206.

[33] *High Frequency Structure Simulator (HFSS) User Guide*. Accessed: Aug. 2019 and Mar. 2021. [Online]. Available: http://www.ansys.com/

[34] M. I. Ibrahim *et al.*, "29.8 THzID: A 1.6 mm^2 package-less cryptographic identification tag with backscattering and beam-steering at 260GHz," in *IEEE ISSCC Dig. Tech. Papers*, Feb. 2020, pp. 24–26.

[35] F. Meng, K. Ma, K. S. Yeo, C. C. Boon, W. M. Lim, and S. Xu, "A 220–285 GHz SPDT switch in 65-nm CMOS using switchable resonator concept," *IEEE Trans. THz Sci. Technol.*, vol. 5, no. 4, pp. 649–651, Jul. 2015.

[36] M. I. W. Khan *et al.*, "CMOS THz-ID: A 1.6-mm^2 package-less identification tag using asymmetric cryptography and 260-GHz far-field backscatter communication," *IEEE J. Solid-State Circuits*, vol. 56, no. 2, pp. 340–354, Feb. 2021.

[37] M. I. W. Khan, S. Kim, D.-W. Park, H.-J. Kim, S.-K. Han, and S.-G. Lee, "Nonlinear analysis of nonresonant THz response of MOSFET and implementation of a high-responsivity cross-coupled THz detector," *IEEE Trans. THz Sci. Technol.*, vol. 8, no. 1, pp. 108–120, Jan. 2018.

[38] X. Yi, C. Wang, X. Chen, J. Wang, J. Grajal, and R. Han, "A 220-to-320-GHz FMCW radar in 65-nm CMOS using a frequency-comb architecture," *IEEE J. Solid-State Circuits*, vol. 56, no. 2, pp. 327–339, Feb. 2021.

[39] C. Wang and R. Han, "Dual-terahertz-comb spectrometer on CMOS for rapid, wide-range gas detection with absolute specificity," *IEEE J. Solid-State Circuits*, vol. 52, no. 12, pp. 3361–3372, Dec. 2017.

[40] G. Bertoni, J. Daemen, M. Peeters, and G. Van Assche. (2011). *The KECCAK Reference*. [Online]. Available: https://keccak.team/files/Keccak-reference-3.0.pdf

[41] H. M. Lee, C. S. Juvekar, J. Kwong, and A. P. Chandrakasan, "A nonvolatile flip-flop-enabled cryptographic wireless authentication tag with per-query key update and power-glitch attack countermeasures," *IEEE J. Solid-State Circuits*, vol. 52, no. 1, pp. 272–283, Jan. 2017.

[42] H. T. Friis, "A note on a simple transmission formula," *Proc. IRE*, vol. 34, no. 5, pp. 254–256, May 1946.

[43] N. B. Simpson, K. Dholakia, L. Allen, and M. J. Padgett, "Mechanical equivalence of spin and orbital angular momentum of light: An optical spanner," *Opt. Lett.*, vol. 22, no. 1, pp. 52–54, Jan. 1997.

[44] N. Biton, J. Kupferman, and S. Arnon, "OAM light propagation through tissue," *Sci. Rep.*, vol. 11, no. 1, Jan. 2021, Art. no. 2407.

[45] R. Neo, S. Leon-Saval, J. Bland-Hawthorn, and G. Molina-Terriza, "OAM interferometry: The detection of the rotational Doppler shift," *Opt. Exp.*, vol. 25, no. 18, pp. 21159–21170, Sep. 2017.

Muhammad Ibrahim Wasiq Khan (Graduate Student Member, IEEE) received the B.E. degree (Hons.) in electrical engineering from the National University of Science and Technology (NUST), Islamabad, Pakistan, in 2012, and the M.Sc. degree in electrical engineering from the Korea Advanced Institute of Science and Technology (KAIST), Daejeon, South Korea, in 2016. He is currently pursuing the Ph.D. degree with the Electrical Engineering and Computer Science (EECS) Department, Massachusetts Institute of Technology (MIT), Cambridge, MA, USA, with a focus on CMOS-based terahertz (THz) identification tags, THz energy harvesting systems, and THz-orbital-angular-momentum (OAM) secure transceivers.

He worked on THz detectors and THz imaging systems based on CMOS technology at KAIST. His research interests include mm-wave and THz integrated wireless systems.

Mr. Khan was a recipient of the IEEE Radio Frequency Integrated Circuits (RFIC) Symposium Best Student Paper Award (First Place) in 2021. He also received the Rector's Silver Medal for his B.E. degree.

Jongchan Woo (Graduate Student Member, IEEE) received the B.S. degree in electrical engineering from the Korea Advanced Institute of Science and Technology (KAIST), Daejeon, South Korea, in 2018, and the M.S. degree in electrical engineering and computer science from the Massachusetts Institute of Technology (MIT), Cambridge, MA, USA, in 2021, where he is currently pursuing the Ph.D. degree with the Electrical Engineering and Computer Science (EECS) Department with a focus on hardware and physical-layer security.

His research interests include low-power circuits and systems and energy-efficient secured hardware.

Xiang Yi (Senior Member, IEEE) received the B.E. degree from the Huazhong University of Science and Technology (HUST), Wuhan, China, in 2006, the M.S. degree from the South China University of Technology (SCUT), Guangzhou, China, in 2009, and the Ph.D. degree from Nanyang Technological University (NTU), Singapore, in 2014.

He was a Post-Doctoral Fellow with the Massachusetts Institute of Technology (MIT), Cambridge, MA, USA. He was also a Research Fellow with NTU from 2014 to 2017. He is currently a Professor with SCUT. His research interests include radio frequency (RF), millimeter-wave (mm-Wave), and terahertz (THz) frequency synthesizers and transceiver systems.

Dr. Yi was a recipient of the IEEE ISSCC Silkroad Award and the SSCS Travel Grant Award in 2013. He is also a technical reviewer for several IEEE journals and conferences.

Mohamed I. Ibrahim (Member, IEEE) received the B.Sc. and M.Sc. degrees in electrical engineering from Ain Shams University, Cairo, Egypt, in 2012 and 2016, respectively, and the M.S. and Ph.D. degrees in electrical engineering and computer science from the Massachusetts Institute of Technology (MIT), Cambridge, MA, USA, in 2020 and 2021, respectively.

He is currently a Staff Design Engineer with MediaTek USA, Irvine, CA, USA. His research interests include microelectronic circuits and systems for high-speed wireless/wireline transceivers and chip-scale quantum systems, as well as novel electromagnetic materials and devices.

Dr. Ibrahim was a recipient of the MIT-MTL Fall-2021 Doctoral Dissertation Award, the 2021 IEEE SSCS Predoctoral Achievement Award, and the 2021 IEEE MTT Graduate Fellowship, among others. He also serves as a technical reviewer for several IEEE journals.

Rabia Tugce Yazicigil (Member, IEEE) received the B.S. degree in electronics engineering from Sabanci University, Istanbul, Turkey, in 2009, the M.S. degree in electrical and electronics engineering from the École Polytechnique Fédérale de Lausanne (EPFL), Lausanne, Switzerland, in 2011, and the Ph.D. degree in electrical engineering from Columbia University, New York, NY, USA, in 2016.

She was a Post-Doctoral Research Associate with the Electrical Engineering and Computer Science (EECS) Department, Massachusetts Institute of Technology (MIT), Cambridge, MA, USA, from 2016 to 2018. She is currently an Assistant Professor with the Electrical and Computer Engineering Department, Boston University, Boston, MA, USA, and a Visiting Scholar with MIT. Her research interests lie at the interface of integrated circuits, signal processing, security, biosensing, and wireless communications to innovate system-level solutions for future energy-constrained applications.

Dr. Yazicigil is also a member of the 2015 MIT EECS Rising Stars Cohort. She was a recipient of a number of awards, including the "Electrical Engineering Collaborative Research Award" for her Ph.D. research on compressive sampling applications in rapid RF spectrum sensing in 2016, the Second Place at the Bell Labs Future X Days Student Research Competition in 2015, the Analog Devices Inc. Outstanding Student Designer Award in 2015, and the 2014 Millman Teaching Assistant Award of Columbia University. She has served as the Vice-Chair of the Rising Stars 2020 Workshop at the IEEE International Solid-State Circuits Conference (ISSCC). She also serves on the Technical Program Committee (TPC) of IEEE ISSCC and IEEE European Solid-State Circuits Conference (ESSCIRC).

Anantha P. Chandrakasan (Fellow, IEEE) received the B.S, M.S., and Ph.D. degrees in electrical engineering and computer sciences from the University of California at Berkeley (UC Berkely), Berkeley, CA, USA, in 1989, 1990, and 1994, respectively.

Since September 1994, he has been with the Massachusetts Institute of Technology (MIT), Cambridge, MA, USA, where he is currently the Vannevar Bush Professor of electrical engineering and computer science. He was the Director of the MIT Microsystems Technology Laboratories from 2006 to 2011. From July 2011 to June 2017, he was the Head of the Department of Electrical Engineering and Computer Science, MIT. Since July 2017, he has been the Dean of the School of Engineering, MIT. He is a coauthor of *Low Power Digital CMOS Design* (Kluwer Academic Publishers, 1995), *Digital Integrated Circuits* (Pearson Prentice-Hall, 2003, second edition), and *Sub-Threshold Design for Ultra-Low Power Systems* (Springer 2006). His research interests include ultra-low-power circuit and system design, energy harvesting, energy-efficient RF circuits, and hardware security.

Dr. Chandrakasan was a co-recipient of several awards, including the 2007 ISSCC Beatrice Winner Award for Editorial Excellence and the ISSCC Jack Kilby Award for Outstanding Student Paper (2007–2009). He received the 2009 Semiconductor Industry Association (SIA) University Researcher Award, the 2013 IEEE Donald O. Pederson Award in Solid-State Circuits, an Honorary Doctorate from KU Leuven in 2016, the UC Berkeley EE Distinguished Alumni Award in 2017, and the 2019 IEEE Solid-State Circuits Society Distinguished Service Award. In 2015, he was elected to the National Academy of Engineering. In 2019, he was elected to the American Academy of Arts & Sciences. He has served in various roles for the IEEE International Solid-State Circuits Conference (ISSCC), including the Program Chair, the Signal Processing Sub-Committee Chair, and the Technology Directions Sub-Committee Chair. He has served as the Conference Chair of ISSCC from 2010 to 2018. He has served as the Senior Technical Advisor to the Conference starting ISSCC 2019. He was elected as a Fellow of the Association for Computing Machinery (ACM) in 2020.

Ruonan Han (Senior Member, IEEE) received the B.Sc. degree in microelectronics from Fudan University, Shanghai, China, in 2007, the M.Sc. degree in electrical engineering from the University of Florida, Gainesville, FL, USA, in 2009, and the Ph.D. degree in electrical and computer engineering from Cornell University, Ithaca, NY, USA, in 2014.

He is currently a tenured Associate Professor with the Department of Electrical Engineering and Computer Science, Massachusetts Institute of Technology, Cambridge, MA, USA. His research interests include microelectronic circuits and systems operating at millimeter-wave and terahertz frequencies.

Dr. Han was a recipient of the Cornell ECE Director's Ph.D. Thesis Research Award, the Cornell ECE Innovation Award, the IEEE Microwave Theory and Techniques Society (MTT-S) Graduate Fellowship Award, the IEEE Solid-State Circuits Society (SSC-S) Predoctoral Achievement Award, the Intel Outstanding Researcher Award in 2019, and the U.S. National Science Foundation (NSF) CAREER Award in 2017. He and his students won three Best Student Paper Awards of the IEEE Radio frequency Integrated Circuits (RFIC) Symposium in 2012, 2017, and 2021. He has served as an Associate Editor for IEEE TRANSACTIONS ON VERY LARGE SCALE INTEGRATION (VLSI) SYSTEMS from 2019 to 2021 and a Guest Associate Editor for IEEE TRANSACTIONS ON MICROWAVE THEORY AND TECHNIQUES in 2019. He has been serving as an Associate Editor for IEEE TRANSACTIONS ON QUANTUM ENGINEERING since 2020. He has served on the Steering Committees of the IEEE International Microwave Symposium in 2019 and 2021. He also serves on the Technical Program Committees of the IEEE RFIC Symposium and the European Microwave Conference. He is also an IEEE MTT-S Distinguished Lecturer for the term 2020–2022.